International Journal of Design & Nature and Ecodynamics
Vol. 21, No. 8, August, 2026, pp. 2381-2394
Journal homepage: http://iieta.org/journals/ijdne

Effect of Air Diffuser Angle on Air Curtain Performance for Salt Wedge Intrusion Control

Ahmed Sami Naser[1*], Basim Sh. Abed[2], Israa Abdulwahab Al-Baldawi[1]

[1] Department of Water Resources Engineering, College of Engineering, University of Baghdad, Baghdad 10071, Iraq
[2] Department of Civil Engineering, Al-Hadi University, Baghdad 10011, Iraq

Corresponding Author Email: Ahmed.Sami2510p@coeng.uobaghdad.edu.iq

https://doi.org/10.18280/ijdne.210819

Received: 20 June 2026
Revised: 19 August 2026
Accepted: 26 August 2026
Available online: 31 August 2026

Keywords:
salt wedge intrusion, air curtain, computational fluid dynamics, air diffuser angle, saltwater transmission, open channel

ABSTRACT

Salt wedge intrusion is an important hydraulic problem in estuaries and open channels, where saltwater moves upstream under the freshwater layer due to the water density difference between them. The numerical model was first validated using laboratory results for a salt wedge without an air curtain. In this study, a three-dimensional, transient model was developed using computational fluid dynamics (CFD) to investigate the effect of three air diffuser angles (90°, 60°, and 30°) on the performance of an air curtain used to reduce salt wedge intrusion. The volume of fluid (VOF) model was used to represent the interaction between freshwater, saltwater, and air. In addition, the Realizable (k−ε) turbulence model was used to represent the turbulence effects within the computational domain. The finding in this study for the numerically calculated salt wedge length was 3.62 m, compared to the laboratory value of 3.705 m, with a relative error of 2.29%. The results showed that the 60° diffuser angle had the best performance among the three tested angles at the present hydraulic and geometric conditions, especially in the initial low-Froude operation stage. In the initial operational stage, this angle recorded the highest prevention efficiency (66.42%) and the shortest time required to break the saltwater wedge (approximately 5.5 sec). Therefore, the 60° diffuser angle can be considered the best-performing configuration among the three tested angles under the present study conditions, mainly due to its faster initial response and lower saltwater transmission during the initial low Fr_{air} stage.

1. INTRODUCTION

Saltwater intrusion is an important hydraulic and environmental problem in estuaries and open channels. It happens due to the density difference between saltwater and freshwater, allowing the denser saltwater to move upstream against the flow of freshwater near the channel bed, forming what is known as a salt wedge. This phenomenon is an environmental and hydraulic problem because it reduces freshwater quality, threatens drinking water and irrigation intakes, and affects environmental balance in estuary areas [1-3]. The extent of the salt wedge is influenced by several factors, most importantly freshwater discharge, density difference, saltwater depth, channel slope, bed roughness, and tides in natural estuaries [4-7].

Previous studies on salt wedges have been classified into four categories: field, experimental, numerical, and control. Field studies investigating the behavior of salt intrusion included data collection and measurement of the salt wedge shape, demonstrating that river flow, bed shape, depth, and tides influence the propagation and shape of the salt wedge. Studies also showed that changes in channel geometry can either increase or decrease the size of the salt wedge [4, 5, 8]. In rivers, during periods of drought, the decrease in freshwater discharge can become the dominant factor influencing the advance of the salt wedge upstream [6, 9, 10].

The second category of studies consists of experimental studies, which are divided into two groups: the first group examined saltwater intrusion within open channels [2] and examined the effects of freshwater discharge, channel bed, slope, saltwater density, and saltwater depth along the length and shape of the salt wedge. The study showed that increasing freshwater discharge and channel slope lead to a reduction in the length of the salt wedge. In other laboratory studies involving the mixing of fresh and saltwater, flow instability and density gradients strongly influence the vertical salinity distribution and the location of the salt wedge [11, 12]. The second group investigated air curtains as a control technique for preventing saltwater intrusion; the study [1] investigated both salt wedge propagation and air curtains under laboratory conditions. The study concluded that hydraulic parameters have an effect on preventing the salt wedge from advancing.

Nakai and Arita [13] conducted experiments to prevent salt intrusion propagation using an air curtain and classified the behavior of the salt wedge around the curtain into different flow patterns based on the balance between the buoyancy force resulting from air bubbles, the force of salt wedge intrusion, and the inertial force resulting from freshwater flow. Their study concluded that, under suitable operating conditions, an air curtain can prevent salt wedge propagation.

Kahrizi et al. [14] used a double air curtain to study its effect in preventing salt wedge propagation. The study concluded that the curtain's effectiveness depends on the saltwater density and freshwater discharge; these are the factors affecting the double curtain's performance. Lu et al. [15] conducted flume experiments under estuary dynamic conditions. The experiments show that air curtains increase vertical mixing and dissipate the momentum of the saltwater flow, thus reducing saltwater intrusion.

In addition to field and experimental studies, analytical and numerical models were used to predict the length of the salt intrusion and the salinity distribution in the channel, including one-dimensional and three-dimensional models without the use of any curtain [9, 10, 16-19]. One such study [16], which is relevant to the Iraqi environment; they used an analytical model to predict salt intrusion in the Shatt al-Arab under different discharge and tidal conditions. The results showed a convergence between the results and the measurements. CFD studies have also shown that numerical models are effective in representing the salt wedge propagation with acceptable accuracy when the boundary conditions are controlled [3, 18].

Regarding the category of studies that addressed controlling or preventing the propagation of the salt wedge, some of these studies suggested increasing freshwater discharge, constructing barriers and gates, modifying the bed roughness, using sills, and using air curtains [20-26]. The use of air curtains is a promising technique, as barriers cause sediment accumulation and reduce navigational depth, while air curtains generate a column of bubbles that change the velocity and turbulence fields, thus preventing the advance of the salt wedge [13, 27, 28].

Previous studies have concluded that air discharge, water depth, density difference, and the location of the air curtain are factors affecting air curtain performance [13, 15, 29-31]. Laboratory studies have shown that an air curtain can prevent or reduce salt wedge propagation when the buoyancy force generated by the bubbles is sufficient to counteract the saline intrusion force [13].

Due to the difficulty of measuring all variables within the bubble zone in the laboratory or field, several studies have used numerical modeling to investigate the performance of the air curtain. One such study [32] simulated the prevention of salt intrusion in the Panama Canal using an air curtain; this study employed the ANSYS Fluent software and a mixing model combined with the k-ε turbulence model. The results showed that the air curtain reduces saline intrusion and that increasing the air velocity leads to increased effectiveness in preventing intrusion.

Naderi et al. [33] also examined the effect of the air curtain in tidal river estuaries using ANSYS Fluent. The aim was to evaluate the effect of air pumping on reducing seawater advance. The study was based on the multiphase flow model and the k-ε model and concluded that increasing air pumping stops the advance of the salt wedge.

Oldeman et al. [30] performed an advanced numerical study of bubble screens for the reduction of salt intrusion in sea locks. The Euler-Lagrange CFD model was used with salt equilibrium representation and density-concentration correlation. The objective was to optimize the bubble curtain design and understand the mixing. The results indicate that the curtain acts as a barrier between salt and fresh water initially, but can become a mixer when the turbulence increases or the curtain oscillates.

Talebi et al. [29] studied numerically the factors affecting the air curtain performance, especially the effects of the density of saltwater and the rate of airflow. The results showed that increasing saltwater density reduces the curtain's effectiveness in preventing salt intrusion and can lead to circulation that promotes salt ingress behind the curtain if the airflow rate is insufficient. The study also indicated that an increase in the airflow rate improves the performance until a certain point, after which the effect becomes negligible. This study underscores the importance of evaluating efficiency not only in terms of reducing salt wedge intrusion but also in terms of the amount of saltwater passing through the curtain.

Table 1. Comparison of selected previous studies on air-curtain control of saltwater intrusion

Study	Air Flow	Diffuser Configuration	Water Depth	Model Type	Main Findings
Nakai and Arita [13]	q = 0–4.17 cm²/s per unit width	Bed-mounted line diffuser; 8-mm pipe, 0.6-mm holes at 10-mm spacing	0.156–0.162 m	Experimental	Adequate airflow could completely arrest the salt wedge; three characteristic flow regimes were identified.
Oldeman et al. [30]	13–107 L/min (Fr_{air} = 0.57–1.15)	PVC and porous-stone spargers; PVC tubes contained 90 holes of 0.8 mm	0.40 m numerical liquid depth	Euler–Lagrange CFD	Maximum mitigation occurred near (Fr_{air} = 0.91); higher airflow increased mixing without further improvement.
Al-Fuady and Azzubaidi [1]	Minimum required (Q = 0.25–1.50) L/min	T-shaped 8-mm pipe; seven 1-mm holes at 10-mm spacing	0.09 m	Experimental	Required airflow increased toward the downstream saltwater source and depended strongly on diffuser location.
Talebi et al. [29]	q = 5×10^{-5}–3×10^{-4} m²/sec	Transverse perforated pipe	0.44 m	Eulerian CFD, RNG (k−ε)	Airflow improved prevention up to an optimum range; increasing seawater density reduced curtain effectiveness.
Kahrizi et al. [14]	Variable; minimum (Q_{air}) for complete control determined as (Q_{air}/Q_{salt})	Two linear curtains at 0.50 and 1.00 m; five 1-mm holes at 10-mm spacing	0.23–0.25 m	Experimental	Curtains closer to the downstream saline source required more airflow; denser saltwater also increased airflow demand.
Lu et al. [15]	0–7.5 L/min	Line-type air-curtain device	0.25 m	Experimental, tidal flume	Increasing airflow reduced salt intrusion, but stronger tidal mixing reduced the relative effectiveness of the curtain.

Raaghav et al. [34] studied bubble curtains in lock-exchange flow by large eddy simulation. The study focused on transient dynamics in the curtain-driven regime. The results showed that air curtain effectiveness changes with time.

Research on bubble columns and two-phase flow shows that the characteristics of the air diffuser, bubble size, and air flow rate control the bubble column width, induced flow velocity, drag, and mixing rates [35, 36]. Rising bubbles can also generate swirling zones on either side of the curtain; these vortices can be beneficial in impeding saltwater intrusion, but they can also cause partial salinity transfer to the freshwater side if the airflow is large or if the curtain's position is unsuitable [15, 29]. Therefore, understanding the relationship between the shape of the air curtain and its resulting velocity field is essential for improving saltwater intrusion prevention efficiency. The main characteristics and findings of selected previous studies on air-curtain control of saltwater intrusion are summarized in Table 1.

Although previous studies have addressed the effects of air discharge, curtain location, saltwater density, channel depth, bubble size, and tidal conditions, the effect of the air injection angle has not received sufficient attention. Most studies have treated the air curtain as a vertical bubble barrier, while the possibility of improving performance by changing the diffuser angle has not been sufficiently investigated. This is because the diffuser's angle can change the momentum distribution between the vertical and horizontal components, affecting the shape of the bubble column, the recirculation area, the velocity field, and the turbulent kinetic energy distribution, and consequently, the amount of saltwater transmitted behind the curtain.

The current study is a numerical evaluation of the effect of the air diffuser angle on the efficiency of an air curtain used to mitigate salt-wedge intrusion in an open-channel flume. Three air diffuser angles, 90°, 60°, and 30° were tested under the same hydraulic conditions and at a fixed curtain location. The curtain was positioned at a specific distance from the saltwater side, representing the controlled salt intrusion length or the design allowable length. Therefore, the comparison between the angles does not depend on the length of the salt intrusion, as this is constant due to the fixed curtain location, but rather on the amount of saltwater passing behind the curtain. The main aims of this study are to compare the hydraulic performance of three selected air diffuser angles (30°, 60° and 90°) and to identify the best-performing angle among the tested configurations under the present operating conditions.

2. METHODOLOGY

2.1 Explanation of the experimental model used for validation

The results of the laboratory study [1] were adopted to validate the ability of the numerical model to simulate the phenomenon of salt wedge intrusion and to compare them with the results of the numerical modeling. This study involved investigating the factors affecting the behavior of the salt wedge within a laboratory flume under different operating conditions. The experiments were conducted in a 6 m long, 7.5 cm wide, and 25 cm high flume supplied with freshwater from the upstream side. On the downstream side, a height-adjustable weir was installed and used to drain the freshwater from the flume, while simultaneously allowing the entrance of saltwater through an opening in its center connected to a saltwater reservoir. This weir retains the saltwater at a specific level that represents the sea level, with the saltwater depth representing the measured distance from the bed of the flume to the top of the weir. To visually distinguish the shape of the salt wedge during the experiments, a small amount of potassium permanganate was added to the saltwater, giving it a distinct purple color and facilitating the observation of its extent and shape within the flume.

2.2 Computational domain

The computational field was established based on the actual dimensions of the laboratory flume used to validate the numerical model. Initially, a basic model of a flume without an air curtain was constructed to compare the simulation results with published laboratory results and to validate the model's ability to represent salt wedge propagation.

The geometric model was drawn using ANSYS SpaceClaim software as a three-dimensional model, with the upstream side representing the freshwater inlet and the downstream side representing the saltwater inlet. The model was based on three phases: freshwater, saltwater, and air, to represent the interaction between the two water layers and the free water surface within the flume.

To reduce the number of computational cells and the solution time, only half the flume width was used by applying the symmetry condition at the longitudinal half-width symmetry plane while maintaining the model's three-dimensional nature. After the validation phase was completed, the computational field was modified by adding an air diffuser at the specified location to study the effect of the air injection angle on the air curtain's efficiency in reducing saltwater intrusion behind it.

2.3 Governing equations

The numerical model developed in this study simulates a three-dimensional, incompressible multiphase flow including air, saltwater, and freshwater phases. The transient formulation of the governing equations is used to track the propagation of the saltwater intrusion and the flow field resulting from air injection. The governing equations include the continuity equation [37], Navier-Stokes equations [37], and volume fraction equation [38]. The continuity equation is given by:

$$\frac{\partial \rho}{\partial t} + \nabla \cdot (\rho u) = 0 \tag{1}$$

where, ρ is the density (kg/m^3), and u is the velocity vector (m/sec). Navier-Stokes equations are given by:

$$\rho\left(\frac{\partial u}{\partial t} + (u \cdot \nabla)u\right) = -\nabla p + \mu \nabla^2 u + \rho g \tag{2}$$

where, μ is the dynamic viscosity (N·sec/m^2), p is the pressure (Pa), g is gravitational acceleration (m/sec^2), and t is the time (sec). The volume fraction transport equation in the VOF model is given by:

$$\frac{\partial \alpha_q}{\partial t} + \nabla \cdot (\alpha_q u) = 0 \tag{3}$$

where, α_q is the volume fraction of phase q, and u is the velocity vector. The numerical model currently utilized is a three-phase VOF formulation with freshwater, saltwater, and air. The liquid phases were defined as two different constant-density liquids, namely freshwater and saltwater, and the gas phase was defined as air. This formulation was employed to track the macroscopic displacement and interface of the saline wedge and its interaction with the air curtain. The volume fraction of the saltwater, α_s, is the fraction of the computational cell occupied by the saltwater. If $\alpha_s = 1$, the cell is filled with the saltwater, whereas if $\alpha_s = 0$, there is no saltwater. Intermediate values ($0< \alpha_s <1$) are interfacial cells and do not have a meaning as local salinity concentration.

Although freshwater and saltwater are physically miscible, molecular salt diffusion and continuous salinity gradients were not explicitly resolved in the present three-phase VOF model. A species-transport approach coupled with a density–salinity relationship would be more suitable for resolving detailed salinity mixing. However, the objective of the present study is to compare the macroscopic hydrodynamic response of the salt wedge and bulk saltwater transmission for different air-injection angles under identical conditions. Therefore, the three-phase VOF approach was retained, and the sharper representation of the freshwater–saltwater interface is acknowledged as a limitation of the present model.

To represent the turbulent effects resulting from the interaction of fresh and salt water, as well as the effect of air injection in the case of an air curtain, the k−ε realizable turbulence model was used. This model was used to calculate the turbulent viscosity and represent the mixing and circulating zones generated within the flume and around the air curtain. k−ε realizable turbulence model [37] is given by:

$$\frac{\partial(\rho k)}{\partial t} + \nabla \cdot (\rho k u) = \nabla \cdot \left[\left(\mu + \frac{\mu_t}{\sigma_k}\right)\nabla k\right] + G_k - \rho\varepsilon \tag{4}$$

$$\frac{\partial(\rho\varepsilon)}{\partial t} + \nabla \cdot (\rho\varepsilon u) = \nabla \cdot \left[\left(\mu + \frac{\mu_t}{\sigma_\varepsilon}\right)\nabla \varepsilon\right] + \rho C_1 S\varepsilon - \rho C_2 \frac{\varepsilon^2}{k+\sqrt{\nu\varepsilon}} \tag{5}$$

$$\mu_t = \rho C_\mu \frac{k^2}{\varepsilon} \tag{6}$$

where, ρ is the fluid density, k is the turbulent kinetic energy, ε is the turbulent dissipation rate, u is the velocity vector, t is the time, μ is the molecular dynamic viscosity, and μ_t is the turbulent viscosity. G_k represents the generation of turbulent kinetic energy due to the mean velocity gradients, while S is the modulus of the mean strain-rate tensor. v is the kinematic viscosity, and σ_k and σ_ε are the turbulent Prandtl numbers for k and ε, respectively. C_1, C_2, and C_μ are model coefficients used in the realizable (k−ε) turbulence model.

2.4 Boundary and initial conditions

The boundary and initial conditions were defined to reproduce the hydraulic conditions of the laboratory flume. The upstream freshwater boundary was specified as a velocity inlet corresponding to the prescribed freshwater discharge, while the downstream saltwater opening was defined as a pressure inlet with a pressure of 1264.23 Pa. The upper open boundary representing the free surface exposed to the atmosphere and the downstream outlet above the weir were specified separately as pressure outlets. The air diffuser openings were defined independently as air velocity inlets. For the inclined diffuser cases, the air-injection direction was aligned with the corresponding diffuser orientation of 30°, 60°, or 90°. The flume bed and side walls were treated as stationary no-slip walls. Because only half of the flume width was modeled, a symmetry boundary condition was applied along the longitudinal vertical plane at the flume centerline (half-width symmetry plane). Gravity was applied in the vertical direction to account for the density difference between freshwater and saltwater.

2.5 Numerical solution method and mesh generation

Numerical simulations were performed using ANSYS Fluent software [39]. A pressure-based solver was employed because the flow in this study was treated as incompressible flow. The simulation was also performed under transient conditions to represent the temporal evolution of the salt wedge and the air curtain flow.

The Volume of Fluid (VOF) model was used to track the interface between the three phases of fluid. A discrete bubble diameter was not defined as an independent model input, since the air phase was explicitly modeled in the three-phase VOF formulation. The k−ε realizable turbulence model was used to represent turbulent momentum transport and the flow structures generated within the computational field, particularly in the freshwater-saltwater interaction region and around the air injection zone.

Pressure and velocity were linked using the PISO algorithm, which is suitable for transient flow simulations. Pressure was discretized using the PRESTO scheme, while the Second-Order Upwind scheme was used to discretize the momentum equations to improve the accuracy of the velocity field calculation. The Geo-Reconstruct scheme was used to solve the volume fraction equation, resulting in a sharper representation of the interface between the phases. A convergence criterion of 10^{-4} was applied to the solved equations.

The numerical field was meshed using the meshing tools available in ANSYS, which gave an adequate representation of the flume geometry and numerical accuracy. Given the importance of the freshwater-saltwater interface and the air diffuser region in air curtain applications. The computational domain was discretized by a three-dimensional mesh, mainly consisting of tetrahedral cells. The basic model without an air curtain had 2,349,823 cells with a general cell size of 5 mm and a refined cell size of 2 mm at the saltwater inlet. In addition, local refinement was carried out around the diffuser and along the air-plume region after the introduction of the air diffuser to more accurately represent the strong gradients in velocity and phase volume fraction. The final air-curtain model contained 2,733,251 cells. A general cell size of 5 mm was used, while the saltwater-inlet region was refined to 2 mm, the region surrounding the diffuser to 1 mm, and the diffuser openings to a minimum cell size of 0.2 mm. The mesh quality was assessed using orthogonal quality, skewness, and aspect ratio. For the air-curtain model, the orthogonal quality ranged from 0.17 to 0.99, the skewness ranged from 3×10^{-5} to 0.82, and the aspect ratio ranged from 1.1 to 9.7. The transient simulations were performed using a time-step size of 0.01 s, with a maximum of 20 iterations per time step. Table 2 summarizes the main geometric, physical, boundary condition, and numerical parameters used in the CFD simulations.

Table 2. Main geometric, physical, boundary condition, and numerical parameters used in the CFD simulations

Category	Parameter	Value / Setting
Geometry	Flume length	6.0 m
	Flume width	0.075 m
	Flume height	0.25 m
Diffuser	Air-curtain location	0.485 m from the weir
	Pipe diameter	0.008 m
	Number of openings	7
	Opening diameter	0.001 m
	Opening spacing	0.010 m
	Injection angles	30°, 60°, 90°
Hydraulic conditions	Freshwater discharge	45.3 L/min
	Flume slope	0%
Fluid properties	Freshwater density	998.2 kg/m³
	Saltwater density	1022.79 kg/m³
	Freshwater viscosity	0.001003 Pa·sec
	Saltwater viscosity	0.001407 Pa·sec
	Air viscosity	1.7894×10^{-5} Pa·sec
Interfacial properties	Air–water surface tension	0.072 N/m
	Freshwater–saltwater surface tension	0.00148 N/m
Air injection	Air injection velocity at diffuser openings	0.66, 1.32, 1.98, 2.65 m/s
	Fr_{air}	0.447, 0.563, 0.645, 0.710
Boundary conditions	Freshwater inlet	Velocity inlet (Q_f = 45.3 lit/min)
	Saltwater inlet	Pressure inlet (1264.23 Pa)
	Diffuser air inlet	Velocity inlet (V_{air} = 0.66, 1.32, 1.98, 2.65 m/s)
	Upper free surface	Pressure outlet
	Outlet over the weir	Pressure outlet
	Flume walls and bed	No-slip wall
	Half-width plane	Symmetry
Numerical model	Multiphase model	Three-phase VOF
	Phases	Freshwater, saltwater, air
	Turbulence model	Realizable k–ε
	Pressure–velocity coupling	PISO
	Pressure discretization	PRESTO!
	Momentum discretization	Second-Order Upwind
	Volume-fraction scheme	Geo-Reconstruct
	Convergence criterion	10^{-4}

Table 3. Mesh- and time-step-sensitivity assessment for the 60° configuration during t = 2–7 sec

Case	Mesh Level	Number of Cells	Time Step (sec)	Averaged Saltwater Mass Flow Rate (kg/sec)	Relative Difference (%)
M1	Coarse	1,763,717	0.01	0.054349	—
M2	Medium	2,733,251	0.01	0.041174	32
M3	Fine	4,701,946	0.01	0.038378	7.29
T1	Medium	2,733,251	0.005	0.042953	4.14

The present study was designed as a controlled comparative CFD investigation aimed specifically at isolating the effect of air-diffuser angle. Therefore, the same mesh strategy, time-step size, boundary conditions, turbulence model, and numerical schemes were applied consistently to all three diffuser-angle cases. The resulting comparisons are thus interpreted as relative differences among the tested configurations under identical computational and hydraulic conditions.

A discretization-independence assessment was performed for a representative 60° air-curtain configuration using three progressively refined meshes and two time-step sizes. The coarse, medium, and fine meshes contained 1,763,717, 2,733,251, and 4,701,946 cells, respectively. All hydraulic conditions, diffuser location, air-injection conditions, boundary conditions, and numerical schemes were kept unchanged during the assessment.

The mean saltwater mass flow rate through the control plane during the initial operating stage, from 2 to 7 seconds, was used as the principal quantity for evaluating discretization sensitivity. The corresponding mean values were 0.054349, 0.041174, and 0.038378 kg/sec for the coarse, medium, and fine meshes, respectively. The relative difference reduced from 32.00% (coarse to medium) to 7.29% (medium to fine). Indicating a clear monotonic convergence trend as the mesh was refined, the results are summarized in Table 3.

Temporal sensitivity was also assessed using the medium mesh by reducing the time-step size from 0.01 sec to 0.005 sec. The corresponding mean saltwater mass flow rates were 0.041174 and 0.042953 kg/s, respectively, giving a relative difference of 4.14%. This result indicates limited sensitivity of the predicted saltwater transmission to further reduction of the time-step size.

Based on these comparisons, the medium mesh and a time-step size of 0.01 sec were retained for the production simulations as a practical balance between numerical resolution and computational cost.

2.6 Model validation

The numerical model was validated by comparing the numerical simulation results with the laboratory results published by research [1]. For this purpose, a basic model was run without the use of an air curtain, under the same hydraulic conditions used in the laboratory experiment. The freshwater discharge for the laboratory experiment used in this study was 45.3 lit/min, the saltwater pressure was 1264.23 Pa, the flume slope was 0%, and the saltwater density was 1022.79 kg/m^3. Validation was performed by comparing the shape and length of the salt wedge generated by the CFD model with the corresponding laboratory values and observations.

The length of the salt wedge in the numerical model was measured from the saltwater inlet at the downstream end to the salt wedge upstream. To calculate the accuracy of the model, the agreement between the numerical and laboratory results was calculated using relative error (RE), root mean square error (RMSE), and skill score (SS). The RE equation [40] is given by:

$$RE = \left|\frac{x_{exp.} - x_{num.}}{x_{exp.}}\right| \times 100 \tag{7}$$

RMSE equation [41] is given by:

$$RMSE = \sqrt{\frac{\sum_{i=1}^{n}\left((x_{num.})_i - (x_{exp.})_i\right)^2}{n}} \tag{8}$$

SS equation [18] is given by:

$$SS = 1 - \frac{\sum_{i=1}^{n}\left((x_{num.})_i - (x_{exp.})_i\right)^2}{\sum_{i=1}^{n}\left((x_{exp.})_i - \overline{x_{exp.}}\right)^2} \tag{9}$$

where, $x_{exp.}$ is the experimental value, and $x_{num.}$ is the numerical value. The interpretation of the skill score is excellent when SS > 0.65, very good when SS is between 0.5 and 0.65, good when SS is between 0.2 and 0.5, and poor when SS < 0.2.

2.7 Simulation cases

The validated CFD model was used after the numerical model validation to investigate the effect of the air diffuser angle on the air curtain performance and its capability to reduce the saltwater intrusion behind it. The three air diffuser angles considered were 90°, 60°, and 30°, with 30° as the nearest angle to the flume bed and 90° as the upward angle. The air curtain was positioned 48.5 cm from the weir, while the flume dimensions, freshwater discharge, saltwater density, flume slope, and numerical solution settings were kept constant for all simulation cases.

The intensity of air injection was expressed as the air Froude number (Fr_{air}), which is a dimensionless measure of the momentum provided by the air curtain to the restoring effect of the difference in density between freshwater and saltwater. The air Froude number was computed as:

$$Fr_{air} = \frac{(g q_{air})^{1/3}}{\sqrt{g' H}} \tag{10}$$

$$g' = g\left(\frac{\rho_s - \rho_f}{\rho_f}\right) \tag{11}$$

where, g is the gravitational acceleration (m/s^2), q_{air} is the airflow rate per unit diffuser width (m^2/sec), H is the water depth (m), g' is the reduced gravitational acceleration (m/s^2), ρ_s and ρ_f are the saltwater and freshwater densities (kg/m^3), respectively.

The purpose of keeping all hydraulic and engineering parameters constant was to isolate the effect of the air injection angle alone on the flow structure and saltwater intrusion control efficiency. Therefore, the comparison between the studied cases is based on the amount of saltwater intruded behind the air curtain across a defined measurement level. This criterion is more appropriate for evaluating the performance of the air curtain in this study, because the curtain's position was fixed and represented the allowable limit or design position for controlling the advance of the salt wedge.

2.8 Efficiency evaluation criterion

The performance of the air curtain was evaluated based on the amount of saltwater transmitted behind the curtain through a specific measuring plane located behind the air injection location, and the air curtain's position was constant in all simulation cases. To evaluate the efficiency of preventing saltwater transfer through the plane, the saltwater flow rate behind the curtain was used as the primary criterion for comparing different air diffuser angles. To determine the flow rate of saltwater passing through the plane behind the curtain, the following equation was used:

$$m_s = \int_A \rho_s \alpha_s (u.n) dA \tag{12}$$

where, m_s is the saltwater mass flow rate behind the air curtain (kg/s), ρ_s is saltwater density (kg/m^3), α_s is saltwater volume fraction, u is the velocity vector (m/s), n is the unit normal vector to the control plane, and A is the area of the control plane (m^2).

Since the flow in the present study is transient, the mean saltwater mass flow rate was used to evaluate the air-curtain performance. The reference baseline ($m_{s,b}$) was obtained from the basic model without an air curtain through the same control plane used for the air-curtain cases. After the salt wedge reached a quasi-steady condition, the mean saltwater mass flow rate through this plane was 0.122623 kg/s, which was adopted as the reference value for the prevention efficiency calculation. The prevention efficiency was calculated using the following equation:

$$E\% = \left(\frac{m_{s,b} - m_{s,i}}{m_{s,b}}\right) \times 100 \tag{13}$$

where, $m_{s,i}$ is the saltwater mass flow rate behind the air curtain at a specific diffuser angle i (kg/s), and $m_{s,b}$ is the reference mean saltwater mass flow rate through the same control plane in the basic model without an air curtain (kg/s). The closer E is to 100%, the greater the reduction in saltwater transmission through the control plane.

The salt-wedge breakup time was determined directly from the temporal saltwater mass flow rate curves at the control plane. To avoid identifying short-lived flow fluctuations as breakup, an objective persistence criterion was adopted. Breakup was defined as the first time at which the saltwater mass flow rate decreased to 1% or less of the reference no-curtain saltwater mass flow rate through the control plane and remained below this threshold for at least 2 sec. With $m_{s,b}$ = 0.122623 kg/s, the corresponding threshold was approximately 1.23×10^{-3} kg/s. This criterion was applied consistently to all three diffuser angle cases.

2.9 Quantitative determination of recirculation-zone dimensions

The recirculation zone was quantified using the streamwise velocity component, u_x, the recirculation zone was quantified using the streamwise velocity component. The main recirculation region was defined as the connected region in which the streamwise velocity was negative ($u_x < 0$), while its boundary was identified by the zero-streamwise-velocity condition ($u_x = 0$). Streamwise velocity profiles were extracted in CFD-Post at several vertical elevations above the flume bed. For each profile, the locations at which the velocity changed sign were determined by linear interpolation between two adjacent points having opposite velocity signs. The zero-crossing location was calculated as

$$X_0 = X_1 - u_1 \frac{X_2 - X_1}{u_2 - u_1} \tag{14}$$

where, X_1 and X_2 are two adjacent streamwise coordinates and u_1 and u_2 are their corresponding streamwise velocity components, with $u_1 u_2 < 0$. For each elevation, the local streamwise extent of the connected negative-velocity region was calculated as:

$$L_r(\mathrm{Y}) = X_R - X_L \tag{15}$$

where, X_L and X_R are the upstream and downstream zero-velocity crossings bounding the main recirculation region. The maximum streamwise extent was then obtained as:

$$L_r = max[L_r(Y)] \tag{16}$$

Because the main recirculation region was attached to the lower flow region near the bed, its maximum vertical extent, H_r, was determined from the highest elevation at which the connected negative-streamwise-velocity region remained present. The upper boundary was therefore bracketed between the highest profile showing reverse flow and the next profile at which the streamwise velocity became positive throughout the corresponding region. Small isolated negative-velocity pockets that were not spatially connected to the main recirculation region were excluded. Considering the local mesh resolution of approximately 5 mm, the final dimensions were reported using meaningful significant digits to avoid implying numerical precision finer than the computational grid.

3. RESULTS and DISCUSSION

3.1 Model validation results

Before investigating the effect of the diffuser angle, the basic model was first simulated in ANSYS Fluent software without the use of an air curtain to represent the development of the salt wedge within the flume. Figure 1 shows the actual laboratory model used in the experimental study, illustrating the extension of the colored salt wedge within the flume.

Figures 2 and 3 show the contour of the saltwater volume fraction generated by the basic numerical model. The figures show the formation of a wedge-shaped saltwater layer near the flume bed, with a gradual increase in the thickness of the salt wedge downstream.

The numerical model was validated using the basic case without an air curtain. The resulting salt wedge profile from the numerical simulation was compared with the corresponding laboratory profile under the same hydraulic conditions, as shown in Figure 4. The comparison showed that the CFD model accurately represented the overall shape and position of the salt wedge.

Figure 1. Salt wedge propagation case study in laboratory

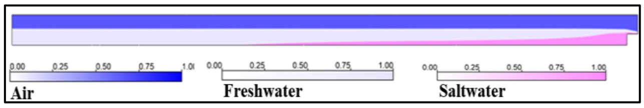

Figure 2. Saltwater volume fraction of the basic numerical model without air curtain

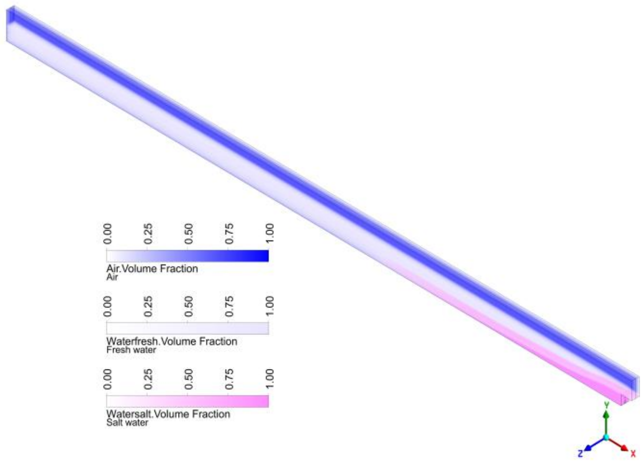

Figure 3. 3D saltwater volume fraction of the basic numerical model without air curtain

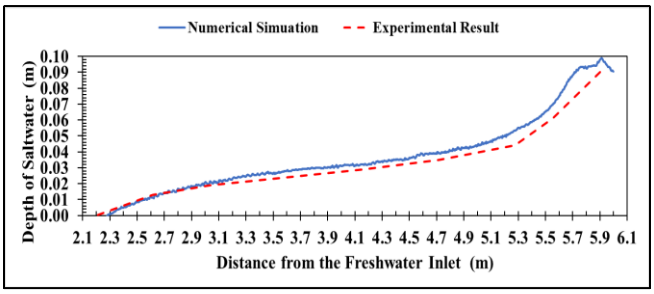

Figure 4. Comparison between the numerical and experimental salt wedge profiles for the validation basic model

The numerically calculated length of the salt wedge was 3.62 m, while the laboratory-measured length was 3.705 m, resulting in a relative error of 2.29%, and the absolute difference for the salt wedge length was 0.085 m, indicating good agreement between the numerical and experimental results. For the height along the salt wedge, the relative error was 10.84%, the RMSE for the salt wedge height was 0.005 m, and the skill factor was 0.96, indicating excellent agreement between the numerical and laboratory results. Therefore, the numerical model can be adopted as a suitable model for simulating the intrusion of the salt wedge into the flume, and then used to study the effect of the air diffuser angle on the performance of the air curtain.

3.2 Reference saltwater flow rate

The basic numerical model without an air curtain was used to determine the reference saltwater mass flow rate for the prevention-efficiency calculations. The saltwater mass flow rate was extracted through the same control plane used for the air-curtain cases, providing a consistent basis for evaluating saltwater transmission under controlled and uncontrolled conditions.

In Figure 5, the variation of the saltwater mass flow rate through the control plane with time for the basic model without an air curtain is shown. The development of the salt wedge caused transient fluctuations in the flow rate, as the saltwater front moved down the flume. As the salt wedge developed fully, the saltwater mass flow rate through the control plane approached a quasi-steady condition. The average mass flow rate of saltwater during this quasi-steady period was 0.122623 kg/s, and this value was used as the reference baseline to calculate the prevention efficiency.

Using the reference value from the same control-plane location ensures that the calculated prevention efficiency corresponds to the reduction in transmission of saltwater caused by the air curtain relative to the corresponding no-curtain condition.

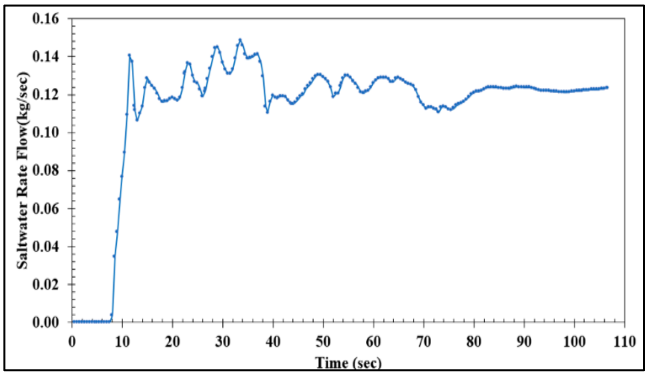

Figure 5. Time-based variation of saltwater mass flow rate through the control plane for the basic model without air curtain

3.3 Effect of air diffuser angle on saltwater transmission

After completing the validation of the basic model for salt wedge intrusion, an air curtain was added to the numerical model in ANSYS Fluent to study the effect of the diffuser angle on the amount of saltwater flow rate behind the curtain. The diffuser was located at a distance of 48.5 cm from the weir, and three air injection angles were tested: 90°, 60°, and 30°. Before quantitatively comparing the angles, a qualitative comparison was performed for the 90° angle at time t = 18.5 s between the numerical simulation results and the corresponding laboratory observation, as shown in Figure 6. This comparison showed that the numerical model could reproduce the main features of the air curtain flow, such as the upward motion of the bubble column and the turbulence of the saltwater layer close to the diffuser.

In addition to the qualitative comparison shown in Figure 6, a quantitative comparison was performed using the minimum airflow required to prevent salt-wedge propagation at the same diffuser location. In the experimental study [2], the minimum air discharge required for prevention was correlated with the diffuser location as $Q_{a,min} = 11.14x^{-0.66}$, where Q_a is the air discharge rate in L/min and x is the distance from the weir in cm. At the diffuser location used in the present study ($x = 48.5$ cm), this relation gives a minimum required airflow of approximately 0.86 L/min, which is close to the experimentally applied value of 0.875 L/min. In the numerical model, an airflow of approximately 0.874 L/min ($Fr_{air} \approx 0.71$) produced nearly complete prevention, with a prevention efficiency of approximately 99.92%. Thus, the numerical model reproduced the experimentally observed airflow level required to suppress salt-wedge propagation at the selected curtain location.

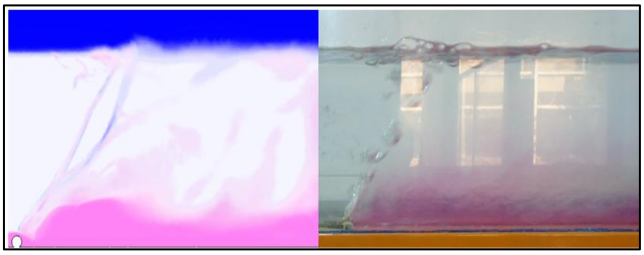

Figure 6. Qualitative comparison between the computational fluid dynamics (CFD) result and laboratory observation for the 90° air curtain case at t = 18.5 s

To measure the amount of saltwater passing behind the air curtain, a control plane was established behind the diffuser location, as shown in Figure 7. From this plane, the mass flow rate of the saltwater was extracted from transient CFD results. This approach allowed for the evaluation of each angle's performance based on the actual amount of saltwater transmitted behind the curtain.

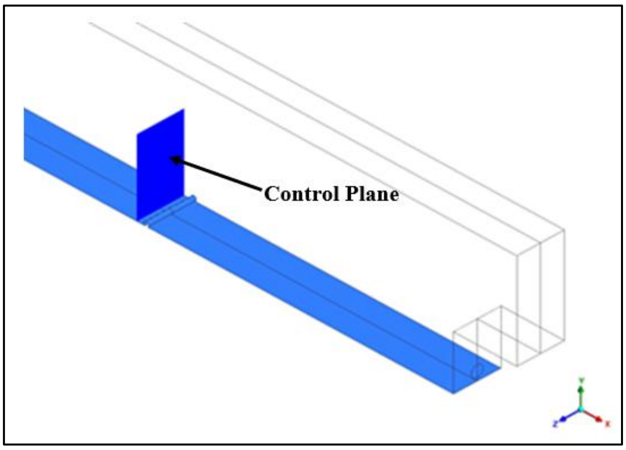

Figure 7. Location of the control plane used to calculate saltwater mass flow rate behind the air curtain

The air curtain was operated using a prescribed stepwise airflow schedule that was identical for all three diffuser angles. Air injection started at t = 2 s, and the air Froude number was successively increased through four operating stages: $Fr_{air} = 0.447$ during 2–7 sec, $Fr_{air} = 0.563$ during 7–12 sec, $Fr_{air} = 0.645$ during 12–17 sec, and $Fr_{air} = 0.710$ during 17–25 sec. Because airflow intensity and elapsed time increased simultaneously, the present simulations do not independently separate the effects of airflow magnitude from the transient start-up response. Therefore, the stage-by-stage results are interpreted primarily as the transient response of the different diffuser angles under the same prescribed airflow schedule, as shown in Figure 8. This division helps in studying the time response of the air curtain and determining how rapidly each angle reduces saltwater transmission during the early and late operational stages.

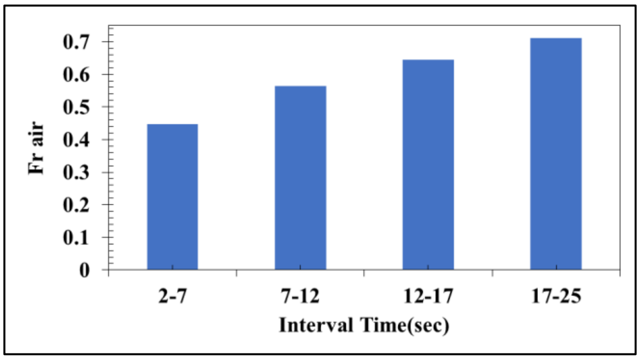

Figure 8. Air Froude number (Fr_{air}) for the four operating time intervals of the air curtain

The mass flow rate of saltwater passing through the control plane behind the curtain was calculated for three air diffuser angles: 90°, 60°, and 30°, as shown in Figures 9, 10 and 11, respectively. The results showed that the air curtain reduced the saltwater flow behind it at all tested angles, but the magnitude of the reduction and the response speed varied with the air diffuser angle.

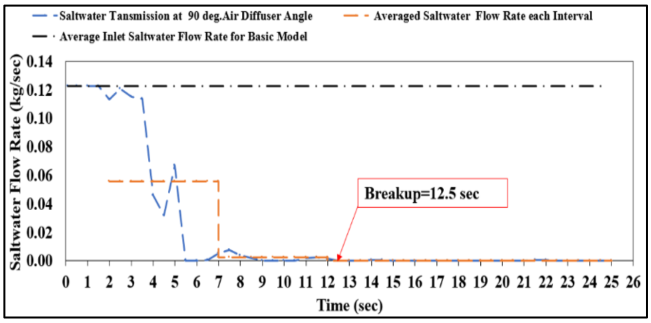

Figure 9. Temporal variation of saltwater mass flow rate through the control plane for the 90° diffuser angles

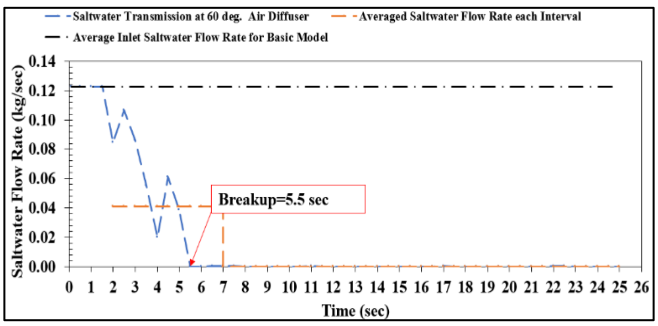

Figure 10. Temporal variation of saltwater mass flow rate through the control plane for the 60° diffuser angles

In the initial stage of air curtain operation, the 60° angle, as shown in Figure 10, exhibited the best performance compared to the other two angles, resulting in the smallest amount of saltwater moving behind the curtain. This indicates that injecting air at the 60° angle generated a more efficient flow structure for lifting and disturbing the saltwater layer before it crossed the control plane. In the 90° case (Figure 9), the bubble column was mainly directed upward, which helped lift the saltwater, but it did not generate sufficient horizontal resistance during the initial stage. In contrast, the 30° angle in Figure 11 exhibited a higher saltwater transmission at the beginning of the simulation. This is attributed to the increased horizontal component of the injection and the resulting unstable circulation, which allows some saltwater to pass behind the curtain.

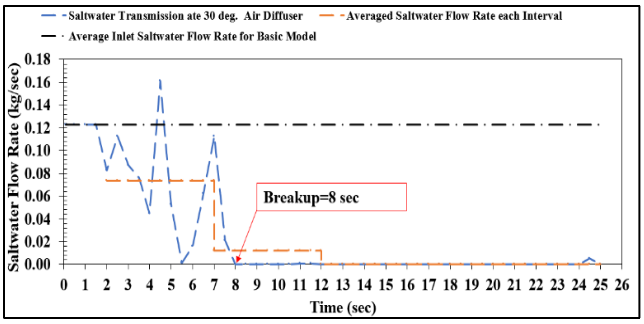

Figure 11. Temporal variation of saltwater mass flow rate through the control plane for the 30° diffuser angles

The temporal saltwater flow rate curves show that the 60° angle reached a lower level of saltwater transmission more quickly than the other angles. But during the critical initial period of operation of the air curtain, the 60° angle responded faster and more efficiently. After stabilization of the flow, all three angles showed reduced saltwater transmission.

3.4 Saltwater mass flow rate and prevention efficiency

The performance of the air curtain was evaluated using the saltwater mass flow rate through the control plane as the primary raw quantity and the prevention efficiency (E) as the normalized performance indicator. The values obtained for all diffuser angles and operating stages are summarized in Table 4.

Figure 12 shows the variation of prevention efficiency with Fr_{air} for the three diffuser angles (90°, 60°, and 30°). In general, as Fr_{air} increased, the amount of saltwater transmitted behind the curtain decreased, and the prevention efficiency increased.

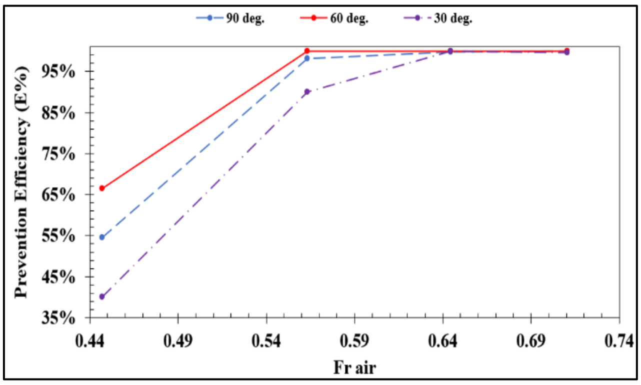

Figure 12. Variation of prevention efficiency (E) with air Froude number (Fr_{air}) for the three diffuser angles

Table 4. Saltwater mass flow rate and prevention efficiency for the tested diffuser angles at different air Froude numbers (Fr_{air})

Stage	Time Interval (sec)	Fr_{air}	Diffuser Angle	Time-Averaged Saltwater Mass Flow Rate ($m_{s,i}$, kg/s)	Prevention Efficiency (E, %)
1	2–7	0.447	90°	0.055812	54.48
1	2–7	0.447	60°	0.041174	66.42
1	2–7	0.447	30°	0.073557	40.01
2	7–12	0.563	90°	0.002299	98.13
2	7–12	0.563	60°	0.000122	99.90
2	7–12	0.563	30°	0.012261	90.00
3	12–17	0.645	90°	0.000281	99.77
3	12–17	0.645	60°	0.000033	99.97
3	12–17	0.645	30°	0.000032	99.97
4	17–25	0.71	90°	0.000096	99.92
4	17–25	0.71	60°	0.000067	99.95
4	17–25	0.71	30°	0.000417	99.66

The results indicated that the best results were achieved when the air curtain angle was 60° at the initial values of Fr_{air}, which is the critical stage that is the beginning of the response of the air curtain to the salt wedge propagation. The prevention efficiency was 54.48%, 66.42%, and 40.01% at the 90°, 60°, and 30° angles, respectively.

The 60° angle resulted in the least amount of saltwater passing behind the curtain during the initial injection stage, while the 30° angle demonstrated the highest relative saltwater transfer. As Fr_{air} increased in the following injection stages, the prevention efficiency increased for all three diffuser angles.

In the second stage, the prevention efficiency reached 98.13% at 90°, 99.90% at 60°, and 90.00% at 30°. This indicates that the 60° angle achieved perfect prevention at a relatively low Fr_{air} value and faster than the other two angles. At higher Frair values, the prevention efficiency for all three diffuser angles approached 100%, indicating very low saltwater transmission through the control plane. This indicates that increasing the air injection intensity further reduces saltwater transmission.

It should be noted that the observed improvement across successive stages cannot be attributed exclusively to increasing Fr_{air}, because the airflow was increased progressively with elapsed simulation time. The comparison among diffuser angles, however, remains consistent because all three configurations were subjected to the same airflow schedule and were evaluated at the same operating stages. The clearest distinction among the tested angles occurred during the initial low Fr_{air} stage, whereas the differences became progressively smaller as the air curtain developed and the prevention efficiency approached 100%.

Although all angles performed better at higher Fr_{air} values, the 60° angle remained the best in terms of initial response, achieving the highest prevention efficiency value at the lower Fr_{air}. This is attributed to the fact that this angle provides a suitable balance between the vertical and horizontal components of air momentum; the vertical component helps to lift the saltwater layer, while the horizontal component contributes to creating a resistance zone against the propagation of the salt wedge. Therefore, the 60° diffuser configuration among the three diffuser angles tested exhibited the most desirable performance under the present conditions, especially during the initial low air Froude number (Fr_{air}) stage. With higher Froude numbers, the differences between the three angles became smaller as all configurations neared complete prevention.

3.5 Flow structure and physical interpretation

The transient response of the air curtain was also evaluated using the salt-wedge breakup time, t_b. Based on the criterion defined in Section 2.8 and the temporal mass flow rate curves shown in Figures 9–11, the salt-wedge breakup times were approximately 12.5 s, 5.5 s, and 8 s for the 90°, 60°, and 30° diffuser angles, respectively. Although short-lived reductions in saltwater mass flow occurred at earlier times in some cases, these were not classified as breakup because the flow subsequently increased above the prescribed threshold are shown in Figure 13. This indicates that the 60° angle not only resulted in the lowest saltwater movement behind the curtain but also was the fastest in weakening the stable structure of the salt wedge.

These results indicate that the 60° configuration provides a favorable balance between the vertical lift generated by the bubble column and the horizontal modification of the flow opposing salt-wedge propagation. Therefore, the combination of a shorter time required to break the saltwater, reduced saltwater flow, and higher prevention efficiency supports the selection of an angle of 60° as the best performance between the three tested diffuser angles in the studied cases.

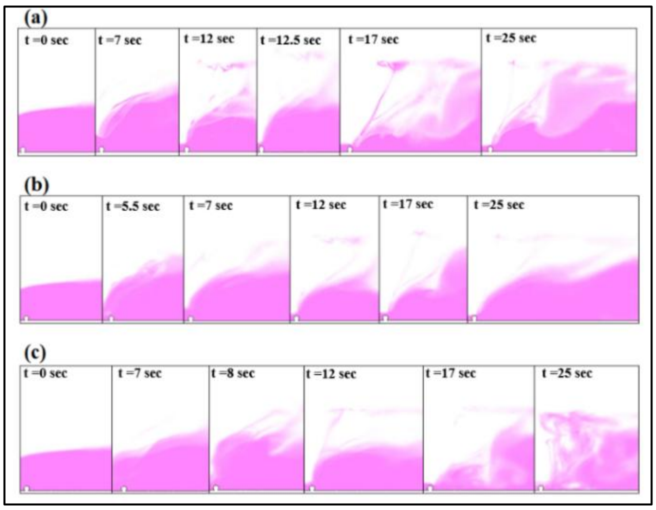

Figure 13. Time required to break the saltwater wedge: (a) 90° air diffuser angle (breakup = 12.5 s), (b) 60° air diffuser angle (breakup = 5.5 s), and (c) 30° air diffuser angle (breakup = 8 s)

Figure 14 shows the longitudinal velocity (u) profile with dimensionless depth (Y/H) at the measurement plane 2 located in front of the air curtain, for angles 90°, 60°, and 30° at (Fr_{air} = 0.71037). Depending on the longitudinal axis used in the model, negative velocity values represent flow in the direction of the salt wedge advance from the saltwater inlet towards the freshwater side, while positive values represent flow in the opposite direction to the salt front's advance. Therefore, the distribution of positive and negative values with depth provides an important indication of the nature of the interaction between the saltwater front and the flow field generated in front of the air curtain.

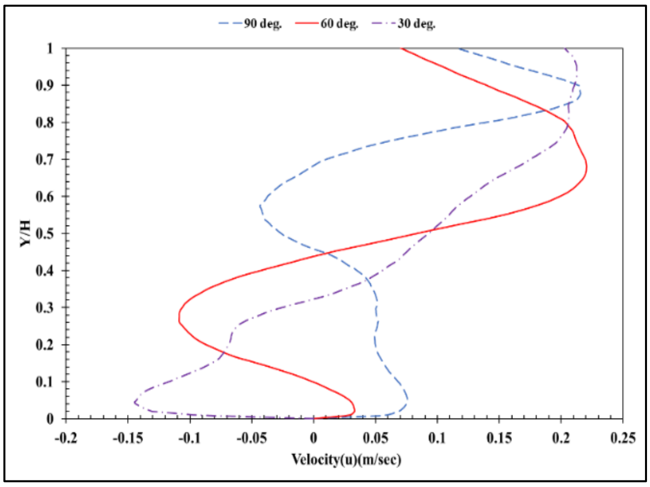

Figure 14. Velocity profile u with dimensionless depth (Y/H) at the measurement plane in front of the air curtain for the 90°, 60°, and 30° diffuser angles at Fr_{air} = 0.71037

For the 30° diffuser angle, Figure 14 shows that the velocity is clearly negative at the lower depth, particularly near the bed, and then gradually becomes positive in the upper layers. This means that the movement near the bed, the main area of salt wedge propagates, remains in the direction of the saltwater front's advance. Although positive values appear in the upper part of the depth, this opposing movement is not concentrated in the most hydraulically important region, i.e., near the bottom. Therefore, a 30° angle does not generate sufficient effective resistance at the underlying saltwater wedge layer, which explains its weak ability to break the saltwater front early and the higher volume of saline transported behind the curtain compared to other cases.

At a 90° angle, however, it exhibits a different velocity distribution. Values are positive near the bed, then a negative region appears in the middle of the depth, before the velocity returns to higher positive values in the upper layers. The positive values near the bed indicate a movement opposing the salt wedge propagation in the lower region, representing a resistive effect against the salt front's movement. However, the presence of a negative region in the middle of the depth means the development of a vertical rotation cell due to the upward movement of the bubble column. This behavior shows that vertical injection mainly depends on vertical uplift and local mixing, circulating some of the saltwater within the depth rather than creating an inclined, extended hydrodynamic barrier. Thus, a 90° angle can weaken the salt wedge, but might allow the transfer or circulation of some of the saltwater movement within the middle layers.

In the case of a 60° angle, the velocity is observed to be close to zero or slightly positive near the bed, then a negative zone appears in the lower to middle depths before becoming increasingly positive in the upper layers. This distribution indicates that the saltwater front is not entirely confined to the bed as in the case of a 30° angle, but rather some of its movement is lifted towards higher layers due to the inclined injection effect. Simultaneously, the large positive values in the upper layers suggest a strong opposing movement or a reorganization of the flow above the reaction zone. Thus, a 60° angle generates a more balanced flow structure, combining the uplift of the saltwater front from the bed region with the formation of a turbulent reaction zone in the lower-middle region, along with upward movement that helps redistribute the flow and reduce the continued advance of the salt wedge.

In general, Figure 14 shows that a 30° angle allows for continued negative movement near the bed, i.e., in the direction of the saltwater wedge propagation, making it the least effective at controlling the saltwater front. A 90° angle generates resistance near the bed but is associated with localized vertical rotation that may transfer some of the saltwater movement to the middle layers. In contrast, a 60° angle provides a good velocity distribution because it does not leave the negative movement concentrated at the bed but rather helps to uplift the reaction zone while generating strong positive movement in the upper layers. This explains the superiority of the 60° angle in reducing saltwater transfer and achieving a shorter saltwater front breaking time compared to the 90° and 30° angles.

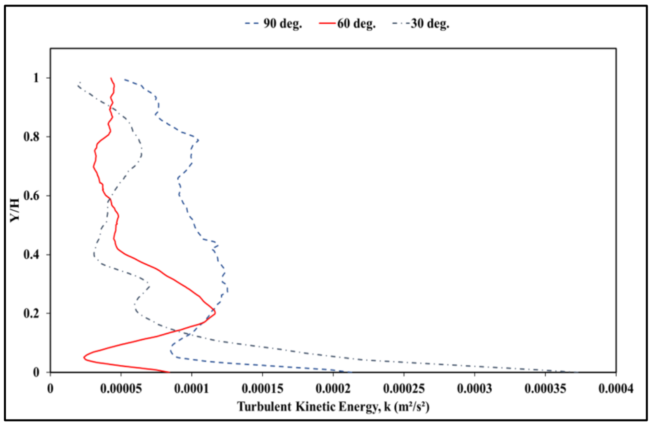

Figure 15. Turbulent kinetic energy (k) profile with dimensionless depth (Y/H) at the measurement plane in front of the air curtain for the 90°, 60°, and 30° diffuser angles at Fr_{air} = 0.71037

Figure 15 shows the turbulent kinetic energy (k) profiles with dimensionless depth (Y/H) at the measurement plane in front of the air curtain for the 90°, 60°, and 30° diffuser angles at Fr_{air} = 0.71037. The profiles show that the diffuser angle affects both the magnitude and vertical distribution of turbulent kinetic energy. For the 30° configuration, the highest k values occur very close to the bed, approximately within Y/H = 0−0.10, followed by a rapid decrease with increasing depth, indicating that the strongest turbulent activity is concentrated within a relatively narrow near-bed region. For the 60° configuration, a noticeable local increase in k occurs within the lower part of the water column, approximately at Y/H = 0.15−0.30, after which the values generally decrease toward the upper layers. In contrast, the 90° configuration maintains comparatively higher k values over a broader vertical region, particularly around Y/H = 0.20−0.40, indicating a wider vertical distribution of turbulent activity. Therefore, although the 60° diffuser does not produce the highest turbulent kinetic energy, its k profile indicates that turbulent activity is maintained within the lower part of the water column. This suggests that the improved salt-wedge control observed at 60° is associated with the distribution of turbulent kinetic energy rather than with its maximum magnitude alone.

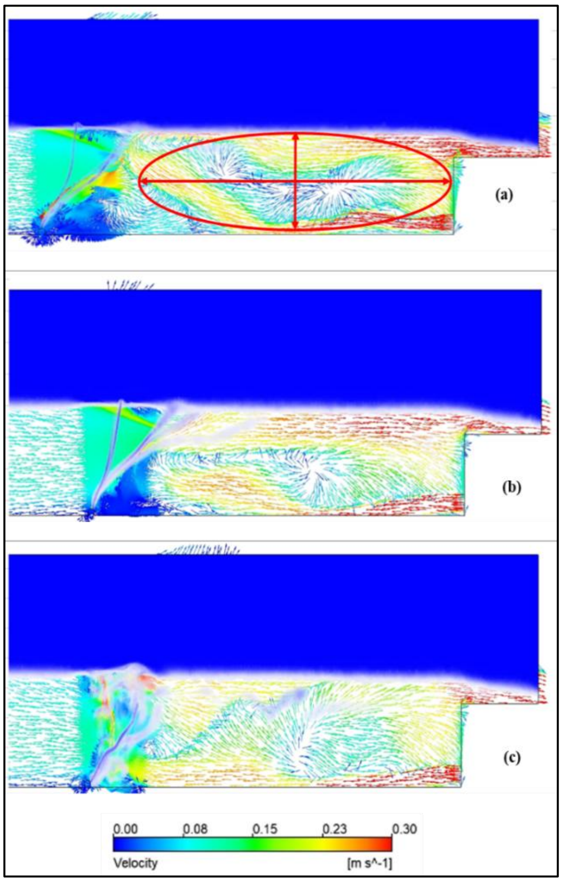

Figure 16. Comparison of the recirculation-zone extent upstream of the air curtain for diffuser angles of (a) 90°, (b) 60°, and (c) 30°

Figure 16 shows the recirculation structures generated in front of the air curtain for the three diffuser angles. The recirculation-zone dimensions were quantitatively determined from the streamwise velocity profiles using the criterion described in Section 2.9. The main recirculation region was defined as the connected region in which the streamwise velocity component was negative ($u_x < 0$), with its boundaries identified by the zero-streamwise-velocity locations ($u_x = 0$).

The quantitative analysis showed that the 60° configuration produced the largest streamwise recirculation extent, with L_r = 0.26 m, followed closely by the 30° configuration with L_r = 0.25 m, whereas the 90° configuration produced L_r = 0.22 m. In contrast, the maximum vertical extent was greatest for the 90° configuration, with H_r = 0.10 m, followed by the 30° configuration with H_r = 0.08 m and the 60° configuration with H_r = 0.06 m.

These results indicate that the diffuser angle affects the geometry and spatial development of the recirculation structure. The 60° configuration promoted the greatest streamwise extension of the reverse-flow region, while the 90° configuration produced the greatest vertical development. These differences indicate that the orientation of the diffuser affects the distribution of the recirculating flow in both the longitudinal and vertical directions. Therefore, the recirculation characteristics should be interpreted together with the saltwater mass-flow rate, prevention efficiency, breakup time, velocity distribution, and turbulent kinetic energy when evaluating the overall hydraulic performance of the air curtain.

3.6 Comparative assessment of the tested air diffuser angles

The best air diffuser angle was determined by combining quantitative performance indicators with hydrodynamic analysis of the flow structure around the air curtain. The comparison included the saltwater mass flow rate behind the curtain, the prevention efficiency (E), the salt wedge breaking time, the velocity profile, the turbulent kinetic energy profile, and the extent of the recirculation zone generated in front of the curtain. Since all cases were studied under the same hydraulic conditions, the same curtain location, and the same range of air diffusers, the difference in performance is mainly attributed to the effect of the air diffuser angle.

The results showed the 60° configuration had the best performance among the three angles tested under the present conditions, with the most obvious advantage in the initial low-Fr_{air} stage; the prevention efficiency of this angle was 66.42%, while for 90° it was 54.48%, and for 30°, it was 40.01%. The 60° angle also had the lowest time-averaged saltwater mass flow rate, which means less saltwater could pass behind the air curtain during the first critical stage of operation. In addition, this angle had the shortest time to break the saltwater wedge, about 5.5 s, versus 12.5 s for the 90° angle and 8 s for the 30° angle. These numerical results indicate that the 60° configuration provided the strongest overall initial response among the three tested angles under the present conditions.

The superiority of the 60° angle can be explained by the momentum distribution generated by the air injection. Inclined injection at this angle provides a vertical component that helps lift and disperse the saltwater layer, while simultaneously providing a suitable horizontal component that influences the approach flow in front of the air curtain and increases the interaction of the bubble column with the salt wedge. The velocity profile showed that this angle generated favorable flow redistribution in front of the curtain, while the turbulent kinetic energy (k) profile showed that turbulent activity was maintained within the lower part of the water column. Although the 60° configuration did not produce the highest k magnitude, its turbulence distribution occurred within the region directly associated with salt wedge propagation.

In contrast, a 90° angle was more dependent on vertical lift and localized mixing resulting from the upward movement of the bubble column. Although this mechanism contributed to weakening the saline front, its effect was more localized around the diffuser and less extended towards the salt wedge propagation. The 30° configuration produced high but strongly localized turbulent kinetic energy near the bed, followed by a rapid reduction with increasing depth. Therefore, its lower overall salt-wedge control performance cannot be attributed simply to insufficient turbulence magnitude, but rather to localized turbulent activity and the different spatial development of the recirculation structure. Based on these results, a 60° angle can be considered the best performance among the three tested for the air curtain under the present hydraulic conditions, particularly during the initial low Fr_{air} stage. This performance was associated with a favorable balance between vertical lift, horizontal flow modification, turbulence generation, and recirculation development. Therefore, the 60° configuration presented the best performance among the three diffuser angles studied under the present hydraulic conditions.

4. CONCLUSIONS

A transient three-dimensional numerical model based on the VOF method was developed to evaluate the effect of air-diffuser inclination on air-curtain control of salt-wedge intrusion in an open channel. The model was validated against published laboratory measurements obtained without an air curtain. The predicted salt-wedge length was 3.62 m, compared with the experimental value of 3.705 m, corresponding to an absolute difference of 0.085 m and a relative error of 2.29%. The comparison of the longitudinal salt wedge profile yielded a relative error of 10.84%, an RMSE of 0.005 m, and a skill score of approximately 0.96, demonstrating that the model reproduced the principal characteristics of salt-wedge intrusion with acceptable accuracy.

The air curtain reduced saltwater transmission at all three diffuser angles, while clear numerical differences in performance were observed among the tested injection directions, particularly during the initial operating stage. The first prevention efficiency was maximum for the 60° diffuser with 66.4% against 54.48% and 40.01% for the 90° and 30° diffusers, respectively. The lowest salt transmission was also obtained, and the shortest salt wedge breakup time was about 5.5 seconds, compared with 12.5 s at 90° and 8 s at 30°.

The hydrodynamic results further showed that the diffuser angle produced distinct distributions of turbulent kinetic energy within the water column. The 30° configuration generated the highest localized k values very close to the bed, whereas the 90° configuration maintained turbulent activity over a broader vertical region. The 60° configuration did not exhibit the highest k magnitude but maintained turbulent activity within the lower part of the water column while also producing favorable flow redistribution and the largest streamwise recirculation extent among the three tested configurations.

These findings indicate that air-curtain performance is governed not by the maximum turbulent kinetic energy alone, but by its spatial distribution together with the associated flow and recirculation structure. The findings presented here are limited to the laboratory-scale geometry and hydraulic conditions investigated, i.e., the 6 m long flume, the fixed freshwater discharge, the saltwater density, the diffuser location, and the three diffuser angles tested. The present simulations do not take into account tidal forcing, variable freshwater discharge, bed roughness, sediment transport, and field-scale estuarine geometry. Thus, the results should not be directly extrapolated to natural estuaries without further investigation. Application of the proposed air-curtain configuration at larger scales requires appropriate scale analysis, additional laboratory confirmation, and numerical simulations covering a wider range of hydraulic and geometric conditions.

ACKNOWLEDGMENT

The authors are thankful to the University of Baghdad, College of Engineering, Department of Water Resources Engineering, for their support.

REFERENCES

[1] Al-Fuady, M.F., Azzubaidi, R.Z. (2021). An experimental study on investigating and controlling salt wedge propagation. IOP Conference Series: Earth and Environmental Science, 779(1): 012079. https://doi.org/10.1088/1755-1315/779/1/012079
[2] Al-Fuady, M.F. (2012). Experimental investigation of salt wedge intrusion control in open channels. M.S. thesis. University of Baghdad. https://libcat.uobaghdad.edu.iq/opacThesis/fullrecr.php?nid=25176&hl=ara.
[3] Shaheed, A.K., Azzubaidi, R.Z. (2022). CFD simulation model of salt wedge propagation. Journal of Engineering, 28(1): 76-85. https://doi.org/10.31026/j.eng.2022.01.06
[4] Yakuwa, I., Ohtani, M. (1986). A salt wedge at the estuary of the Ishikari River in Hokkaido. Bulletin of the Faculty of Engineering, Hokkaido University, 130: 1-15.
[5] Jang, D., Hwang, J.H., Park, Y.G., Park, S.H. (2012). A study on salt wedge and river plume in the Seom-Jin River and estuary. KSCE Journal of Civil Engineering, 16(4): 676-688. https://doi.org/10.1007/s12205-012-1521-9
[6] Yuill, B., Brown, G.L., Krolopp, E., Laurent, H., Ramirez, D. (2023). Dynamics of the saltwater wedge in the lowermost Mississippi River during the 2022 low flow season. In SEDHYD Conference Report, 2023: 1-13.
[7] Geyer, W.R., MacCready, P. (2014). The estuarine circulation. Annual Review of Fluid Mechanics, 46: 175-197. https://doi.org/10.1146/annurev-fluid-010313-141302
[8] Yakuwa, I., Takahashi, S., Ohtani, M. (1988). Observations of saline water intrusion at estuaries with salt wedges. Memoirs of the Faculty of Engineering, Hokkaido University, 17(3): 307-315.
[9] Krvavica, N., Ružić, I. (2020). Assessment of sea-level rise impacts on salt-wedge intrusion in idealized and Neretva River Estuary. Estuarine, Coastal and Shelf Science, 234: 106638. https://doi.org/10.1016/j.ecss.2020.106638
[10] Rodrigues, M., Fortunato, A.B., Freire, P. (2019). Saltwater intrusion in the upper Tagus estuary during droughts. Geosciences, 9(9): 400. https://doi.org/10.3390/geosciences9090400
[11] Ibrahim, Z., Abdul Latiff, A.A., Ab Halim, A.H., Abu Bakar, N., Subramaniam, S. (2008). Experimental studies on mixing in a salt wedge estuary. Malaysian Journal of Civil Engineering, 20(2): 188-199. https://doi.org/10.11113/mjce.v20.15766
[12] Xia, W., Zhao, X., Zhao, R., Zhang, X. (2019). Flume test simulation and study of salt and fresh. Water, 11(3): 584. https://doi.org/10.3390/w11030584
[13] Nakai, M., Arita, M. (2002). An experimental study on prevention of saline wedge intrusion by an air curtain in rivers. Journal of Hydraulic Research, 40(3): 333-339. https://doi.org/10.1080/00221680209499947
[14] Kahrizi, E., Neyshabouri, S.A.A.S., Zeynolabedin, A., Souri, J., Akbari, H. (2023). Experimental evaluation of two-layer air bubble curtains to prevent seawater intrusion into rivers. Journal of Water and Climate Change, 14(2): 543-558.

https://doi.org/10.2166/wcc.2023.384
[15] Lu, C., Gao, S., Kang, Y., Yang, Y., Liu, B. (2024). Experimental study of air curtains blocking saltwater intrusion under estuary dynamic conditions. Ocean Engineering, 309(P2): 118562. https://doi.org/10.1016/j.oceaneng.2024.118562
[16] Abdullah, A.D., Gisen, J.I., van der Zaag, P., et al. (2016). Predicting the salt water intrusion in the Shatt al-Arab estuary using an analytical approach. Hydrology and Earth System Sciences, 20(10): 4031-4042. https://doi.org/10.5194/hess-20-4031-2016
[17] Haddout, S., Maslouhi, A., Igouzal, M. (2017). Predicting of salt water intrusion in the Sebou River Estuary (Morocco). Journal of Applied Water Engineering and Research, 5(1): 40-50. https://doi.org/10.1080/23249676.2015.1124029
[18] Zhang, W., Feng, H., Zheng, J., et al. (2013). Numerical simulation and analysis of saltwater intrusion lengths in the pearl River Delta, China. Journal of Coastal Research, 29(2): 372-382. https://doi.org/10.2112/JCOASTRES-D-12-00068.1
[19] Chen, W.B., Liu, W.C., Hsu, M.H. (2015). Modeling assessment of a saltwater intrusion and a transport time scale response to sea-level rise in a tidal estuary. Environmental Fluid Mechanics, 15(3): 491-514. https://doi.org/10.1007/s10652-014-9367-y
[20] Alwan, I.A., Azzubaidi, R.Z. (2021). A computational fluid dynamics investigation of using large-scale geometric roughness elements in open channels. Journal of Engineering Baghdad, 27(1): 35-44. https://doi.org/10.31026/j.eng.2021.01.03
[21] Alwan, I., Mohd Sidek, L., Azzubaidi, R.Z., Al-Sulttani, A.O. (2025). The effect of large-scale engineered roughness elements on the hydraulics of the Shatt al-Arab estuary: Methodology. IOP Conference Series: Earth and Environmental Science, 1545(1): 012115. https://doi.org/10.1088/1755-1315/1545/1/012115
[22] Badr, S.H., Azzubaidi, R.Z. (2023). Using CFD modeling to simulate the control of the propagation of salt wedge using inclined roughness elements. In E3S Web of Conferences, 427: 04008. https://doi.org/10.1051/e3sconf/202342704008
[23] Ali, A.A., Al Thamiry, H.A. (2021). Controlling the salt wedge intrusion in Shatt Al-Arab River by a barrage. Journal of Engineering, 27(12): 69-86. https://doi.org/10.31026/j.eng.2021.12.06
[24] Hendrickx, G.G., Manuel, L.A., Pearson, S.G., Aarninkhof, S.G., Meselhe, E.A. (2024). An earthen sill as a measure to mitigate salt intrusion in estuaries. Estuaries and Coasts, 47(5): 1199-1208. https://doi.org/10.1007/s12237-024-01359-2
[25] Qiu, W., Zhu, J., Luan, H., Qu, G. (2025). Saltwater intrusion and emergency freshwater release in the Changjiang River Estuary under extreme drought. Water Resources Research, 61(8): 123. https://doi.org/10.1029/2025WR040033
[26] Chang, Y., Chen, X., Liu, D., Tian, C., Xu, D., Wang, L. (2023). Study on the control of saltwater intrusion using subsurface dams. Water, 15(22): 3938. https://doi.org/10.3390/w15223938
[27] Abraham, I.G., Van Der Burgh, P., De Vos, I.P. (1973). Pneumatic barriers to reduce salt intrusion through locks. In RIJKSWATERSTAAT Communications. https://repository.tudelft.nl/record/uuid:e3e1ba53-8f09-43c1-8247-7c032b8604c2.
[28] Keetels, G., Uittenbogaard, R.O.B., Cornelisse, J., Villars, N., Pagee, H.V.A.N. (2011). Field study and supporting analysis of air curtains and other measures to reduce salinity transport through shipping locks. Irrigation and Drainage, 60(1): 42-50. https://doi.org/10.1002/ird.679
[29] Talebi, A., Neyshabouri, S.A.A.S., Khoshgou, H. (2022). Investigation on factors affecting the performance of the air bubble curtain in preventing the penetration of salinity. International Journal of Environmental Science and Technology, 19(11): 10599-10612. https://doi.org/10.1007/s13762-022-04232-6
[30] Oldeman, A.M., Kamath, S., Masterov, M.V., et al. (2020). Numerical study of bubble screens for mitigating salt intrusion in sea locks. International Journal of Multiphase Flow, 129: 103321. https://doi.org/10.1016/j.ijmultiphaseflow.2020.103321
[31] Van der Ven, P.P.D., Oldenziel, G. (2018). A scale model study assessing the performance of a bubble screen mitigating salinity driven lock exchange. In Proceedings of the 5th IAHR Europe Congress-New Challenges in Hydraulic Research and Engineering, Trento, Italy, pp. 673-674. https://doi.org/10.3850/978-981-11-2731-1_219-cd
[32] Naderi, M.N., Zolfaghari, O. (2017). Numerical simulation of prevention of saltwater intrusion in Panama channel by using of bubble curtain system. Journal of Applied Research in Water and Wastewater, 8(2): 363-369. https://doi.org/10.22126/ARWW.2017.800
[33] Naderi, M.N., Reza, M., Kermani, H., Barani, G. (2013). Application of bubble curtain system for prevention of seawater intrusion in estuary of tidal rivers. Annals of Biological Research, 4(5): 28-38.
[34] Raaghav, S.K.R., Driessen, R.J.A., O'Mahoney, T.S.D., et al. (2025). Bubble curtains in a lock-exchange flow: The importance of transient dynamics in the curtain-driven regime. arXiv preprint arXiv:2511.23421. https://doi.org/10.48550/arXiv.2511.23421
[35] Fraga, B., Stoesser, T. (2016). Influence of bubble size, diffuser width, and flow rate on the integral behavior of bubble plumes. Journal of Geophysical Research: Oceans, 121(6): 3887-3904. https://doi.org/10.1002/2015JC011381
[36] Zhang, W., Zhu, D.Z. (2013). Bubble characteristics of air–water bubbly jets in crossflow. International Journal of Multiphase Flow, 55: 156-171. https://doi.org/10.1016/j.ijmultiphaseflow.2013.05.003
[37] Malalasekera, W. (1995). Computational Fluid Dynamics (1st ed.). Addison Wesley Longman Limited.
[38] Hirt, C.W., Nichols, B.D. (1981). Volume of fluid (VOF) method for the dynamics of free boundaries. Journal of Computational Physics, 39(1): 201-225. https://doi.org/10.1016/0021-9991(81)90145-5
[39] ANSYS, Inc. (2022). Ansys Fluent tutorial guide. Release 2022 R2. Canonsburg, PA, USA. http://www.ansys.com.
[40] Rice, J.A. (2007). Mathematical statistics and data analysis. Thomson Higher Education, Belmont.
[41] Chai, T., Draxler, R.R. (2014). Root mean square error (RMSE) or mean absolute error (MAE) arguments against avoiding RMSE in the literature. Geoscientific Model Development, 7: 1247-1250. https://doi.org/10.5194/gmd-7-1247-2014